Near-atomic structure of jasplakinolide-stabilized malaria parasite F-actin reveals the structural basis of filament instability

Sabrina Pospich[a], Esa-Pekka Kumpula[b,c], Julian von der Ecken[a], Juha Vahokoski[b,c,d], Inari Kursula[b,c,d,1], and Stefan Raunser[a,1]

[a]Department of Structural Biochemistry, Max Planck Institute of Molecular Physiology, 44227 Dortmund, Germany; [b]Biocenter Oulu, University of Oulu, 90220 Oulu, Finland; [c]Faculty of Biochemistry and Molecular Medicine, University of Oulu, 90220 Oulu, Finland; and [d]Department of Biomedicine, University of Bergen, 5009 Bergen, Norway

Edited by Thomas D. Pollard, Yale University, New Haven, CT, and approved August 21, 2017 (received for review May 5, 2017)

During their life cycle, apicomplexan parasites, such as the malaria parasite *Plasmodium falciparum*, use actomyosin-driven gliding motility to move and invade host cells. For this process, actin filament length and stability are temporally and spatially controlled. In contrast to canonical actin, *P. falciparum* actin 1 (*Pf*Act1) does not readily polymerize into long, stable filaments. The structural basis of filament instability, which plays a pivotal role in host cell invasion, and thus infectivity, is poorly understood, largely because high-resolution structures of *Pf*Act1 filaments were missing. Here, we report the near-atomic structure of jasplakinolide (JAS)-stabilized *Pf*Act1 filaments determined by electron cryomicroscopy. The general filament architecture is similar to that of mammalian F-actin. The high resolution of the structure allowed us to identify small but important differences at inter- and intrastrand contact sites, explaining the inherent instability of apicomplexan actin filaments. JAS binds at regular intervals inside the filament to three adjacent actin subunits, reinforcing filament stability by hydrophobic interactions. Our study reveals the high-resolution structure of a small molecule bound to F-actin, highlighting the potential of electron cryomicroscopy for structure-based drug design. Furthermore, our work serves as a strong foundation for understanding the structural design and evolution of actin filaments and their function in motility and host cell invasion of apicomplexan parasites.

F-actin | *Plasmodium* | cryo-EM | jasplakinolide | malaria

Actin is a highly conserved protein abundantly expressed in almost all eukaryotic cells. In concert with a multitude of actin-binding proteins (ABPs), it is involved in many important biological processes, including cell motility, muscle contraction, and vesicle trafficking (1). After the discovery and first purification of actin from muscle by Straub in 1942 (2), it took almost 50 years until the first crystal structure of monomeric globular actin (G-actin) in complex with DNase I was solved (3). Since then, structural models of filamentous actin (F-actin) have been determined either from medium-resolution electron cryomicroscopy (cryo-EM) maps (4, 5) or by interpreting X-ray fiber diffraction data (6), each of which has certain limitations. The introduction of new direct electron detectors finally enabled the determination of near-atomic structures of mammalian F-actin by cryo-EM (7, 8).

Unicellular eukaryotic apicomplexan parasites, such as species of the genera *Plasmodium*, *Cryptosporidium*, and *Toxoplasma*, require actin for efficient host cell invasion (9, 10). Apicomplexan actin is part of a molecular machine called the glideosome. Myosin A, in combination with several glideosome-associated proteins, interacts with actin to create the force needed for gliding. Details of the underlying mechanism, however, are only partly understood (11, 12). While most apicomplexan parasites express only one actin isoform, *Plasmodium falciparum* has two different actins (13, 14). *Plasmodium* actin 1 is expressed throughout the life cycle and is closely related to the single actin isoform found in other apicomplexan parasites (15). It shares 93% of its sequence with the actin of *Toxoplasma gondii* (16). *Plasmodium* actin 2 is only present in life cycle stages involved in transmission through the mosquito, including the gametocytes and sporozoites (15, 17, 18), and cannot be substituted by actin 1 in gametogenesis (19). Both *Plasmodium* actin isoforms are among the most divergent identified in one organism, sharing less than 80% of their sequence with each other as well as with opisthokont (animal and yeast) and plant actins (14).

Monomeric *P. falciparum* actin 1 (*Pf*Act1) shares its fold with mammalian G-actin (19). Despite this similarity, there are small but appreciable structural deviations, especially at the binding interface of ABPs and the nucleotide-binding pocket. Furthermore, the contact sites important for filament formation contain notable deviations, particularly within the DNase-1–binding loop (D-loop) which is essential for polymerization (4).

Although all apicomplexan parasites express actin, it has been difficult to directly visualize actin filaments in vivo. Besides one recent study that reported an actin-based cytoskeleton in maturing *P. falciparum* gametocytes using superresolution microscopy (20), studies of other stages of the parasites describe shorter filamentous structures in equilibrium with high concentrations of G-actin (21–25). Stabilization of *Plasmodium* actin filaments using high concentrations of the actin-filament stabilizing agent jasplakinolide (JAS) inhibits parasite growth and impairs host cell invasion (26). Thus, it has been proposed that the unstable nature of apicomplexan actin filaments is essential for parasite survival (9). These in vivo findings are supported by several

Significance

The malaria parasite *Plasmodium falciparum* actively invades host cells, using a mechanism that relies on the interaction of the motor protein myosin and actin filaments which serve as tracks. We determined the structure of stabilized *P. falciparum* actin 1 filaments at near-atomic resolution using single-particle electron cryomicroscopy. The high resolution of the structure allowed us to identify important positions in the filament that are essential for the temporal and spatial control of actin polymerization and play a pivotal role in host cell invasion, and thus infectivity. In general, our study provides important insights into the structural design of actin filaments.

Author contributions: I.K. and S.R. designed research; S.P., E.-P.K., J.v.d.E., and J.V. performed research; S.P. analyzed data; and S.P., I.K., and S.R. wrote the paper.

The authors declare no conflict of interest.

This article is a PNAS Direct Submission.

Data deposition: The electron density map after postprocessing has been deposited in the Electron Microscopy Data Bank (EMDB accession code 3805). The final model containing five actin subunits and three jasplakinolide molecules was submitted to the Protein Data Bank, www.pdb.org (PDB ID code 5OGW).

[1]To whom correspondence may be addressed. Email: inari.kursula@uib.no or stefan.raunser@mpi-dortmund.mpg.de.

This article contains supporting information online at www.pnas.org/lookup/suppl/doi:10.1073/pnas.1707506114/-/DCSupplemental.

in vitro studies, in which isolated apicomplexan actins ineffectively polymerized into labile, short filaments (9, 19, 27).

*Pf*Act1 filaments can be stabilized also in vitro with JAS (19, 28), a cyclic peptide originally isolated from the marine sponge *Jaspis johnstoni* (29). Similar to the competitively binding phalloidin, which has a weaker effect on parasite actin (30), JAS dramatically reduces the critical concentration of actin subunits necessary to drive polymerization and stabilizes filaments (28, 31). JAS-stabilized *Pf*Act1 filaments are suitable for electron microscopy studies, as shown by negative staining (30) and cryo-EM reconstructions of *Pf*Act1 filaments (19). Despite the limited resolution of the maps, it was shown that the helical rotation angle of JAS-stabilized *Pf*Act1 filaments (−167.5°) slightly deviates from the one of canonical mammalian skeletal muscle F-actin (−166.6°), indicating possible different interactions of the actin subunits within the filament (19, 30). Biochemical studies on *Pf*Act1 and *T. gondii* actin filaments indicated that the D-loop, as well as an interface once called hydrophobic plug (4) [subsequently referred to as "plug" because of its hydrophilic nature (5,7)], have an impact on the filament stability (9, 19). However, the structural basis of filament instability of *Pf*Act1, which plays a pivotal role in host cell invasion, and thus infectivity, remains poorly characterized, largely because high-resolution structures of *Pf*Act1 filaments were missing.

Here, we report the near-atomic structure of JAS-stabilized *Pf*Act1 filaments at an average resolution of 3.8 Å, determined by cryo-EM. We identify several small but crucial differences compared with canonical actins at inter- and intrastrand contact sites as the probable cause for the instability of the parasite actin filament. Small differences are sufficient to weaken key interactions at the plug and D-loop regions. We further show that JAS binds at regular intervals inside the filament to three adjacent F-actin subunits, occupying a hydrophobic groove that matches its shape. It reinforces intra- and interstrand contacts and, in addition, directly compensates for weak spots in *Pf*Act1 filaments.

Results and Discussion

Structure Determination. Without stabilizing agents, only short, irregular filaments and aggregates of *Pf*Act1 are observed in negative-stain electron microscopy (9, 19). To exclude the possibility that the staining procedure, including a pH shift to pH 4–5 and drying of the sample, disrupts existing but labile filaments, we vitrified nonstabilized *Pf*Act1 filaments and analyzed them by cryo-EM (Fig. S1). Although we screened different conditions, we could only identify short, irregular filaments and fragments, indicating that the staining procedure is not the cause for the instability of the *Pf*Act1 filaments. Because these short, irregular filaments and fragments are not suitable for data collection and processing, we stabilized *Pf*Act1 filaments with JAS for cryo-EM, as described previously (19, 30). This resulted in long, straight filaments, in which single actin subunits could already be distinguished on the micrograph level, illustrating their regular arrangement within a double-stranded helix (Fig. S2*A*).

We collected a cryo-EM dataset and processed it using a single-particle–based approach with external constraints and a priori values that account for the filament character (details are provided in *Materials and Methods*). The constrained refinement converged into a homogeneous Gaussian distribution of projection angles around the equator (Fig. S2*B*). In the case of filaments, the reported average resolution is often affected by the edges, which are prone to processing artifacts, and the internal flexibility of the protein (32). This is also true for the 3D reconstruction of *Pf*Act1 filaments (Fig. 1*A*). Although the average resolution is 3.8 Å, the local resolution of the central fraction is between 3.2 Å and 3.6 Å (Fig. S2 *C* and *D*). Based on the observed resolution gradient, we built an atomic model for the central part of the filament only, containing five actin subunits (Fig. 1 *A* and *B*). We could clearly identify map density corresponding to ADP and the coordinated cation, most probably Mg^{2+} (Fig. 1*C*). The coordination within the nucleotide-binding site of filamentous *Pf*Act1 is remarkably similar to that of canonical

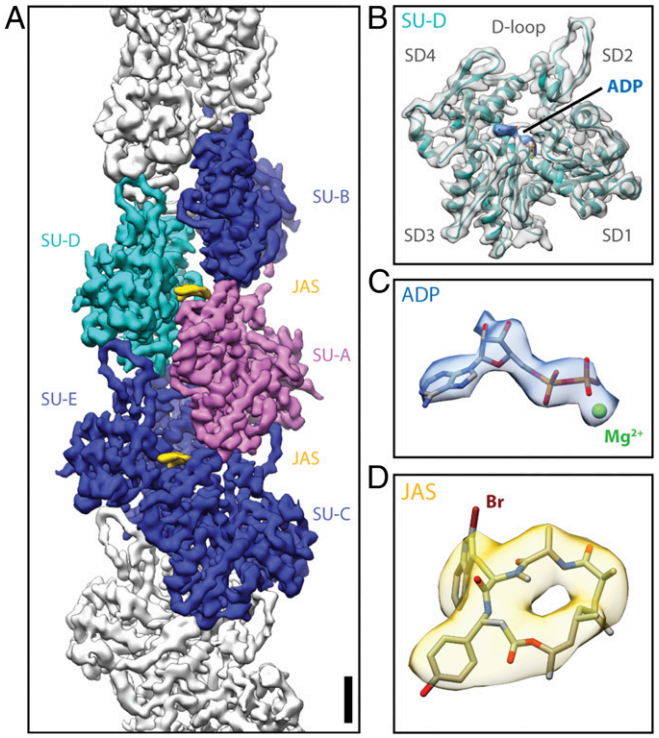

Fig. 1. Structure of JAS-stabilized *Pf*Act1 filament. (*A*) Cryo-EM reconstruction of *Pf*Act1 (gray, with five central subunits in blue, cyan, and magenta) stabilized by JAS (yellow). (*B*) Side view of subunit D (density: gray, atomic model: cyan) with bound ADP (blue) illustrating the SD organization of actin. A close-up view of ADP-Mg^{2+} (*C*) and a slightly tilted top view of JAS (*D*) are shown with respective densities. (Scale bar, 1.5 nm.)

F-actin (Fig. S3). In addition, JAS could be assigned to map densities residing at the center of the filament, intercalating between actin subunits (Fig. 1 *A* and *D*). The orientation of JAS within the map is unambiguous, although the bromine moiety is underrepresented, most likely due to radiation damage (Fig. 1*D*).

Filament Architecture and Interfaces in *Pf*Act1. Filamentous JAS-stabilized *Pf*Act1 arranges in a polar double-stranded helix (Fig. 1*A*) and shares its general filament architecture with mammalian F-actin (7). As reported previously (19, 30), however, the helical rotation angle (also known as the helical twist, dφ) of JAS-stabilized *Pf*Act1 is −(167.5 ± 0.1)°, deviating from the value for canonical actin of −166.6° by ∼1°. The helical rise, dz, of (27.42 ± 0.02) Å is similar to canonical actin. Previously, the helical symmetry was refined using a single-particle–based helical reconstruction approach (19). In our case, since we built our atomic model into a nonsymmetrized (C1) electron density map at 3.8 Å resolution, we could determine the helical symmetry parameters of the filament in an alternative way and just overlay the subunits of the model. In general, the values describing the helical symmetry directly depend on the pixel size, which is difficult to determine accurately. A standard method to measure the pixel size of a given microscope setup is to use a calibration specimen with known dimensions. Depending on the specimen, the inaccuracy of the derived value can be as large as 1–5%. Since the pixel size has a noteworthy impact on the helical symmetry parameters, it is best to compare parameters retrieved from the same microscope setup. For a direct comparison, we therefore determined the helical symmetry parameters of an atomic model of canonical F-actin, originating from a dataset that was collected on the same microscope using comparable settings (results will be published elsewhere). The dz of this model is (27.4 ± 0.1) Å, and the dφ is −(166.6 ± 0.1)°. These values correspond well with the helical symmetry parameters of F-actin that

have been independently determined by different groups (6, 8). We conclude from this that the calibration of our electron microscope is accurate and the twist of *Pf*Act1 filaments is indeed ∼1° larger than in previously determined canonical F-actin structures.

The interface of the two strands within the filament changes slightly due to the altered twist. However, when examining the structures in more detail, we did not observe striking differences that might have an effect on the stability of the filament. All major interactions at the interfaces are present (Fig. S4). Only the position of the D-loop is clearly shifted relative to the position in canonical F-actin (Fig. 2). However, the hydrophobic interaction at this site with the adjacent actin subunit is not affected, and therefore cannot account for the inherent instability of *Pf*Act1 filaments (Fig. S4 *C* and *D*). The different position of the D-loop, which is also the least conserved region of *Pf*Act1, is likely not the cause for the different helical twist. Namely, the D-loop in *Plasmodium* actin 2 is nearly identical in sequence with *Pf*Act1, yet actin 2 filaments have the conventional twist (19). Conversely, the repositioning of the D-loop could be a consequence of the larger twist. On the other hand, replacement of the D-loop in *Pf*Act1 with that of mammalian actin leads to more stable filaments, which, however, still have the twist of 167.5° (19). Thus, if and how the position of the D-loop and the unusual helical twist in *Pf*Act1 filaments are correlated remain to be investigated.

The subdomain (SD) organization of filamentous *Pf*Act1 (Fig. 1*B*) resembles that of the recent structure of canonical F-actin in the ADP state (7). All major intra- and interstrand interfaces reported for canonical F-actin are structurally conserved in *Pf*Act1. These include the plug region in SD3, which is involved in mainly electrostatic interactions between the two strands (Fig. S4 *A* and *B*). The D-loop in SD2 connects by hydrophobic interactions to a complementarily shaped groove in SD3 of an adjacent subunit within the same strand. This contact is furthermore enforced by Y170, which inserts into the D-loop, resembling a lock-and-key interaction (Fig. S4 *C* and *D*). In addition, there are two hydrophobic contact sites that have not been described previously. The first interface consists mainly of V288 in SD3, which enters a shape-complementary groove in SD4 of the adjacent intrastrand subunit (Fig. S5*A*). The second one is in close vicinity and is made up of residues 195–202 of SD4, which interact with SD1 of the opposing interstrand subunit (Fig. S5*B*).

Conformational Change upon Transition Between Globular and Filamentous *Pf*Act1. The canonical actin monomer undergoes a conformational change upon polymerization. During the transition from G-actin to F-actin, SD1 and SD2 rotate by ∼20° relative to SD3 and SD4, resulting in a flattening of the protomer (6, 7). When comparing the globular conformation (19) with the filamentous conformation of *Pf*Act1, we observed that it underwent a similar conformational change (Fig. S6). During the transition from globular *Pf*Act1 to its filamentous form, the monomer rotates by ∼11.5° (Fig. S6 *C* and *D*). The rotation is noticeably smaller than in canonical actin. However, in the crystal structure of globular *Pf*Act1, the SDs are already rotated by ∼7° relative to canonical G-actin. This could be an intrinsic feature of *Pf*Act1 and could be responsible for the higher hydrolysis rate in the G-form compared with canonical G-actin (19). On the other hand, it could also indicate a certain degree of flexibility of monomeric actin. In this line, a recent study on MamK, an actin homolog from bacteria, revealed monomers with different interdomain angles within one crystal (33). Such a difference in conformation or higher degree of flexibility could also reflect a different dependence between ATP hydrolysis and polymerization in the early-branched actins (19). In addition, the smaller difference in conformation between the free actin monomer and the subunit in the filament may contribute to the instability of the filaments by favoring depolymerization.

JAS-Binding Mode. JAS binds at regular intervals inside the filament connecting three actin subunits that span both strands (Figs. 1*A* and 3*A* and Movie S1). It therefore mediates additional intra- and interstrand contacts. This is in agreement with previous molecular modeling studies (34). However, the proposed binding site and orientation of JAS differ substantially. JAS snugly fits into a complementarily shaped groove formed by the interface of SD4 of one subunit and SD3 of the adjacent intrastrand subunit. Its cyclic ring stacks onto a plateau formed by residues 198–202 of SD4 of the first subunit. The aromatic side chains of JAS enter between the two strands, separating SD4 of the same subunit and SD1 of the opposing interstrand subunit (Fig. 3 and Movie S1).

The interactions between JAS and the *Pf*Act1 filament are of a hydrophobic nature. Hydrophobic and weakly soluble in water (29, 35), JAS binds to prominent hydrophobic patches inside the actin filament (Fig. S7). Interestingly, the hydrophobic patches are highly conserved in sequence, explaining the universal stabilizing effect of JAS on many F-actins, including those from green algae and higher plants (19, 28) (Fig. S8). It has been reported that JAS influences at least the dynamic properties, thermal stability, and ATP hydrolysis rate of actin (36, 37). The structures of JAS-stabilized *Pf*Act1 and canonical F-actin, however, are remarkably similar. It would therefore be tempting to speculate that JAS does not alter the filament architecture. Structures of alternatively stabilized *Pf*Act1 filaments and JAS-stabilized canonical actin, however, will be needed to prove this.

Comparison of JAS-Stabilized *Pf*Act1 and Canonical Actin Filaments. To understand which residues are responsible for the inherent instability of *Pf*Act1 filaments and how it is overcome by the binding of JAS, we compared the atomic model of JAS-stabilized *Pf*Act1 with the atomic model of canonical F-actin in detail [Protein Data Bank (PDB) ID code 5JLF] (7, 32). Note that the sequence of *Pf*Act1 is shifted by one amino acid relative to skeletal muscle α-actin from *Oryctolagus cuniculus*. A comparison of the backbone of both models revealed that the only large difference between them is the position of the D-loop (Fig. 2 and Fig. S9). This is surprising, since the protein sequences also differ

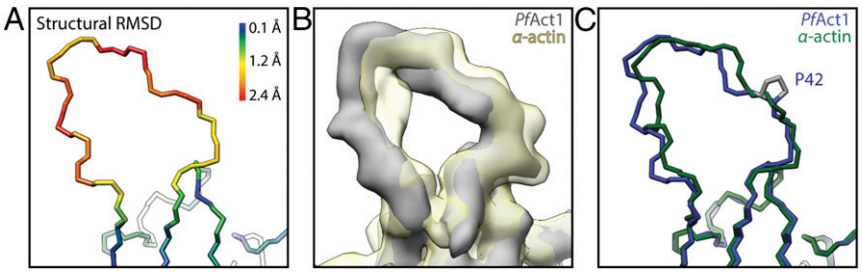

Fig. 2. Structurally deviating D-loop in *Pf*Act1. (*A*) Backbone of the central subunit colored by the root mean square deviation (RMSD) between *Pf*Act1 and α-actin [PDB ID code 5JLF (32)], illustrating a significant deviation within the D-loop. (*B*) Superimposed electron density maps of *Pf*Act1 (gray) and α-actin (yellow) [EMDB accession code 8162 (32)]. (*C*) Backbone of corresponding atomic models in blue and green, respectively [α-actin: PDB accession code 5JLF (32)]. The observed differences within the D-loop originate most likely from P42 in *Pf*Act1 at the position of Q41 in α-actin that introduces a kink.

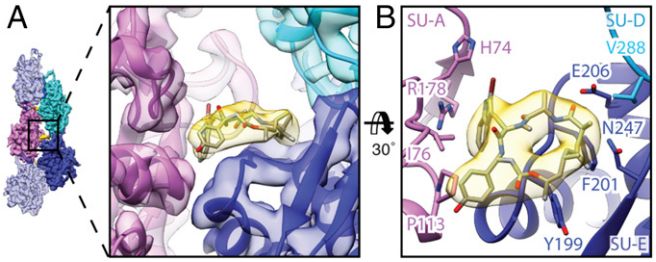

Fig. 3. Interaction of JAS with *Pf*Act1. (*A*) JAS (yellow) binds noncovalently to three actin subunits (magenta, blue, and cyan) strengthening both interstrand and intrastrand contacts. (*B*) Tilted top view of JAS and amino acids involved in the interaction.

in many other regions between *Pf*Act1 and canonical actin (Fig. S9*B*). The D-loop of filamentous *Pf*Act1 is clearly shifted outward relative to the one of canonical actin (Fig. 2*B*). This shift is possibly due to a substitution of Q41 to proline that introduces a kink (Fig. 2*C*). Although this shift has no direct influence on the interface (Fig. S4 *C* and *D*), it might still slightly destabilize the intrastrand contact at this site and weaken the overall stability of the filament. In this line, a D-loop mutant, in which the complete D-loop of *Pf*Act1 was exchanged for that of canonical actin, formed filaments also in the absence of any stabilizing agent (19).

Interestingly, while the tip of the D-loop interacts hydrophobically with the adjacent intrastrand subunit in both actins (Fig. S4), the outward-facing base of the D-loop is negatively charged in *Pf*Act1 and neutral to positive in canonical F-actin (Fig. S10). Although this may not have any effect on the stability of the filament itself, the change of charge likely has an impact on the interactions of *Pf*Act1 with ABPs, particularly coronin and myosin. Both bind to F-actin at the position of or in close vicinity to the D-loop (32, 38, 39).

A detailed inspection of the other interfaces revealed additional small but important differences within the plug region and the JAS-binding site of *Pf*Act1 that probably affect the stability of the filament. The plug region is the major interstrand contact in F-actin and relies on electrostatic complementary surface potentials (5, 7). The general arrangement of the plug and the interaction with the adjacent actin subunit are conserved in JAS-stabilized *Pf*Act1 filaments (Fig. 4 and Fig. S4 *A* and *B*). The interaction is weaker, however, in *Pf*Act1 because a substitution of M269 in canonical F-actin by K270 in *Pf*Act1 results in an inversion of the electrostatic potential and, consequently, repulsion at this site and weakening of the interaction (Fig. 4 *A*, *B*, *D*, and *E*). Although the double-point mutation G200S/K270M for *Pf*Act1 did not result in long filaments in the absence of any stabilizing agent (19), previous studies on actin from *T. gondii* demonstrated a point mutation of K270 to methionine increased the stability of filaments in the presence of a low amount of phalloidin (9). This indicates that this site is indeed important for filament stability. However, its optimization alone is not sufficient to compensate for the instability induced by weaker interactions at other sites.

At the position of amino acids R39 and H40 in the plug region of canonical F-actins, there is a lysine and an asparagine in *Pf*Act1, respectively. Since lysine is less bulky than arginine, this results in an opening of the groove, in which glutamate E271 from the opposing subunit enters, weakening the key-and-lock interaction (Fig. 4 *A*, *C*, *D*, and *F*). Asparagine, instead of histidine, deteriorates the electrostatic interactions at this site. Both residues are located at the base of the D-loop, indicating that not only weaknesses at the tip of the D-loop but also those at its lower part can account for filament instability. This also explains the relatively strong stabilizing effect of the above-mentioned D-loop mutant, in which the complete D-loop of *Pf*Act1 was exchanged for that of canonical actin (19).

We found two additional interfaces that are probably destabilized in *Pf*Act1 filaments compared with canonical F-actin (Figs. 5 and 6). In canonical F-actin, a hydrophobic key-and-lock interaction of I287 located in SD3 with a shape-complementary groove in SD4 strengthens the intrastrand contact (Fig. 5*A*). In *Pf*Act1, this isoleucine is replaced by valine, which is still hydrophobic but less bulky. Consequently, it does not match the shape of the groove and is a greater distance away from the hydrophobic interface (Fig. 5*B*). By binding to both interstrand subunits, JAS reinforces the interaction that is weakened in *Pf*Act1, explaining its stabilizing effect (Fig. 5*C*).

A prominent hydrophobic patch on SD4 spans the inward-directed surface of canonical F-actin and interacts with a hydrophobic region on SD1 of the opposing interstrand subunit (Figs. 5*A* and 6*A*). While the opposing surface is the same in *Pf*Act1, the surface of SD4 is less hydrophobic. This is mainly due to a substitution of T194 and V201 by histidine and serine, respectively. In addition, S199 is replaced by a glycine (G200) that is less bulky, and thus reduces the surface available for the interaction as well as consequently weakening the interaction at

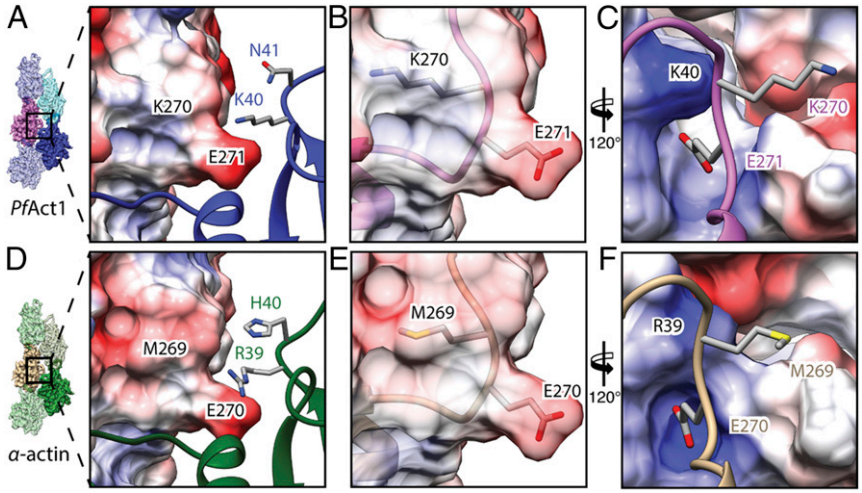

Fig. 4. Weaker interaction of the plug in *Pf*Act1. Comparison of the plug region of *Pf*Act1 (*A*–*C*) and α-actin (*D*–*F*) [PDB accession code 5JLF (32)]. (*D*–*F*) Electrostatic interactions involving R39, H40, and M269 stabilize the interstrand contact of α-actin. (*A*–*C*) Substitution of these residues to lysine, asparagine, and lysine, respectively, weakens this interface in *Pf*Act1. Actin is depicted as surface colored by electrostatic Coulomb potential ranging from −10 kcal·mol^{-1} (red) to +10 kcal·mol^{-1} (blue) or as a ribbon in the color of the respective subunit.

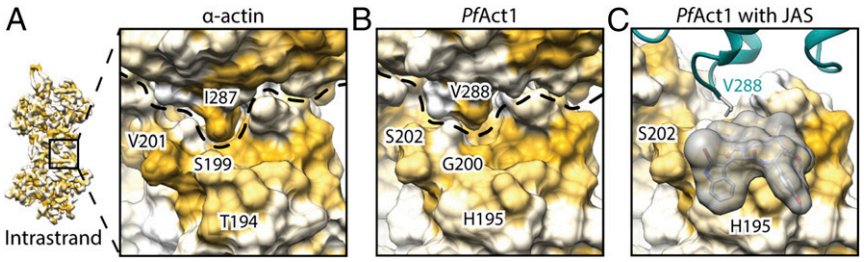

Fig. 5. Destabilized intrastrand contact near JAS-binding site in *Pf*Act1. (*A*) In α-actin, I287 insets into a groove of the adjacent intrastrand subunit resembling a lock-and-key interaction. (*B*) In *Pf*Act1, isoleucine is replaced by valine, resulting in a weaker intrastrand interaction. (*C*) JAS (gray) binds close to this intrastrand contact, reinforcing the interface. Surfaces are colored from high (yellow) to low (white) hydrophobicity. Dashed lines indicate boundaries of actin subunits.

this site (Figs. 5*B* and 6*B*). Supporting this observation, phalloidin-stabilized F-actin from *T. gondii* could be further stabilized by replacing G200 by serine (9). In *Pf*Act1, however, the double-point mutation G200S/K270M did not result in stable filaments (19), indicating that stabilizing the filament only at one position cannot compensate for the instabilities in other regions as discussed above. Interestingly, JAS binds exactly at the interface between SD1 and SD4 (Fig. 6*C*). Since it is hydrophobic itself, it most likely compensates for the loss of hydrophobicity at this interface, and thereby stabilizes the interstrand contact.

To support our structural observations, we performed an in silico analysis of the energy landscape at the binding interfaces. The contribution of a certain side chain to an interaction can be evaluated by calculating the free energy change, ΔΔG, arising from a mutation to alanine. We used Robetta to calculate an in silico alanine scan (40, 41) for *Pf*Act1 and α-actin (Fig. S11). As expected from the comparison of the structures, the energy change at the plug interface is more prominent for α-actin (Fig. S11*D*), indicating a stronger interaction than in *Pf*Act1 (Fig. S11*A*). The hydrophobic key-and-lock interaction near the JAS-binding site (Fig. 5 and Fig. S5) is also weaker for *Pf*Act1 (Fig. S11 *B* and *E*), whereas the D-loop interface of *Pf*Act1 resembles the one of α-actin (Fig. S11 *C* and *F*).

Concluding Remarks

The overall structure of *Pf*Act1 filaments is very similar to that of canonical F-actin. However, several small but important differences at the intra- and interstrand interfaces can be pinpointed as being associated with the inherent filament instability (Table S1). This also highlights the high sensitivity of F-actin to small alterations at important interfaces. JAS not only directly compensates for these weak spots but also stabilizes the filament in general by mediating additional inter- and intrastrand contacts. Our findings deepen our understanding of actin filaments in general and lay the structural foundation for further biochemical studies evaluating the impact of specific residues. It is hoped that this will expand the current model of motility and host cell invasion by *Plasmodium* and apicomplexan parasites in general. It is likely that *Pf*Act1 filaments are stabilized in vivo by other proteins. A temporally regulated stabilization of filaments by, for example, coronin, glideosome-associated connector (42), or myosin could lead to longer filaments when required during the parasite life cycle. Thus, further work is needed to elucidate the exact binding modes of these F-actin–binding proteins on parasite actin filaments.

Importantly, our structure of a small molecule bound to F-actin also highlights the potential of cryo-EM for structure-based drug design directed to F-actin. Studying small molecules in complex with F-actin at atomic resolution is of particular interest. The high similarity of actins from different species requires the exact tailoring of drugs to avoid nonspecific binding. *Pf*Act1 itself could be considered a possible target, taking into account the importance of gliding motility for the life cycle of *Plasmodium*.

Materials and Methods

Details are provided in *SI Materials and Methods*.

***Pf*Act1 Expression, Purification, and Polymerization.** *Pf*Act1 was expressed and purified essentially as described previously (19) and polymerized for 16 h at 20 °C by adding F-buffer components to a final composition of 10 mM Hepes (pH 7.5), 0.2 mM $CaCl_2$, 50 mM KCl, 4 mM $MgCl_2$, 5 mM DTT, and 0.5 mM ATP. In JAS-stabilized samples, JAS (Sigma) was included at a 1:1 molar ratio to actin during polymerization.

Grid Preparation and Image Acquisition for JAS-Stabilized *Pf*Act1. An initial sample check and empirical adjustment of the protein concentration were performed using a standard negative staining protocol described previously (7). For cryosample preparation, the protein sample was first incubated on a previously glow-discharged carbon grid (C-Flats 2/1; Protochips), manually blotted, and finally plunged into liquid ethane for vitrification using a cryoplunger Cp3 (Gatan). Following sample optimization, the final dataset was collected on an FEI Titan Krios transmission electron microscope corrected for spherical aberration (Cs) and equipped with a Falcon2 direct detector (FEI) and an XFEG (FEI) operated at 300 kV.

Image Processing. Images were manually inspected and drift-corrected using Unblur and Summovie (43). Selection of particles was performed manually with sxhelixboxer in SPARX (44), and CTFFIND4 (45) was used for contrast transfer function (CTF) estimation. An initial 3D reference was created from

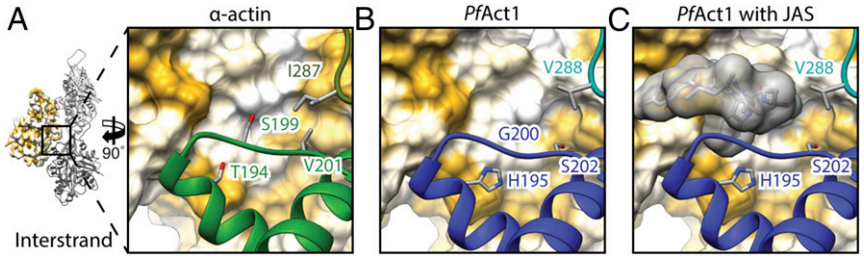

Fig. 6. Destabilized interstrand contact near JAS-binding site in *Pf*Act1. (*A*) Interstrand contact of α-actin is mediated by the hydrophobic residues V201 and T194 (Fig. 5*A*). (*B*) Hydrophobicity is reduced in *Pf*Act1 due to substitutions to serine and histidine, respectively, resulting in a destabilized interface (Fig. 5*B*). (*C*) JAS (gray) binds at this interface and strengthens the interstrand contact. Surfaces are colored from high (yellow) to low (white) hydrophobicity, and ribbons are depicted in the color of the respective subunit.

a homology model of *Pf*Act1 (discussed below) using CHIMERA (46) and SPARX. The refinement and postprocessing were performed with RELION 1.4 (47) in combination with additional restraints to account for the filament character.

Model Building and Refinement. A homology model of filamentous *Pf*Act1 was created using Modeler (48) with canonical F-actin [PDB ID code 5JLF (32)] as a reference structure. This model was flexibly fitted using iModFit (49) before it was refined in real space using PHENIX (50). Further refinement was performed manually using Coot (51) to minimize model bias. An initial model of JAS was generated using Grade.globalphasing (52) and manually refined in Coot. The final refinement and validation were performed using REFMAC (53). The data statistics are summarized in Table S2.

ACKNOWLEDGMENTS. We thank O. Hofnagel for his valuable assistance in electron microscopy and F. Merino for the lively exchange regarding image processing. S.P. and J.v.d.E. are fellows of Studienstiftung des deutschen Volkes. This work was supported by the Max Planck Society (S.R.); the European Council under the European Union's Seventh Framework Programme (FP7/2007–2013) (Grant 615984 to S.R.); the Academy of Finland (Grants 257537, 265112, and 292718 to I.K.); and the Emil Aaltonen, Sigrid Jusélius, and Jane and Aatos Erkko Foundations (I.K.).

1. Pollard TD (2016) Actin and actin-binding proteins. *Cold Spring Harb Perspect Biol*, 10.1101/cshperspect.a018226.
2. Straub FB (1942) Actin. *Stud Inst Med Chem Univ Szeged* II:3–15.
3. Kabsch W, Mannherz HG, Suck D, Pai EF, Holmes KC (1990) Atomic structure of the actin: DNase I complex. *Nature* 347:37–44.
4. Holmes KC, Popp D, Gebhard W, Kabsch W (1990) Atomic model of the actin filament. *Nature* 347:44–49.
5. Fujii T, Iwane AH, Yanagida T, Namba K (2010) Direct visualization of secondary structures of F-actin by electron cryomicroscopy. *Nature* 467:724–728.
6. Oda T, Iwasa M, Aihara T, Maéda Y, Narita A (2009) The nature of the globular- to fibrous-actin transition. *Nature* 457:441–445.
7. von der Ecken J, et al. (2015) Structure of the F-actin-tropomyosin complex. *Nature* 519:114–117.
8. Galkin VE, Orlova A, Vos MR, Schröder GF, Egelman EH (2015) Near-atomic resolution for one state of F-actin. *Structure* 23:173–182.
9. Skillman KM, et al. (2011) Evolutionarily divergent, unstable filamentous actin is essential for gliding motility in apicomplexan parasites. *PLoS Pathog* 7:e1002280.
10. Drewry LL, Sibley LD (2015) Toxoplasma actin is required for efficient host cell invasion. *MBio* 6:e00557.
11. Heintzelman MB (2015) Gliding motility in apicomplexan parasites. *Semin Cell Dev Biol* 46:135–142.
12. Kumpula E-P, Kursula I (2015) Towards a molecular understanding of the apicomplexan actin motor: On a road to novel targets for malaria remedies? *Acta Crystallogr F Struct Biol Commun* 71:500–513.
13. Wesseling JG, de Ree JM, Ponnudurai T, Smits MA, Schoenmakers JG (1988) Nucleotide sequence and deduced amino acid sequence of a Plasmodium falciparum actin gene. *Mol Biochem Parasitol* 27:313–320.
14. Wesseling JG, Smits MA, Schoenmakers JG (1988) Extremely diverged actin proteins in Plasmodium falciparum. *Mol Biochem Parasitol* 30:143–153.
15. Wesseling JG, et al. (1989) Stage-specific expression and genomic organization of the actin genes of the malaria parasite Plasmodium falciparum. *Mol Biochem Parasitol* 35:167–176.
16. Dobrowolski JM, Niesman IR, Sibley LD (1997) Actin in the parasite Toxoplasma gondii is encoded by a single copy gene, ACT1 and exists primarily in a globular form. *Cell Motil Cytoskeleton* 37:253–262.
17. Deligianni E, et al. (2011) Critical role for a stage-specific actin in male exflagellation of the malaria parasite. *Cell Microbiol* 13:1714–1730.
18. Andreadaki M, et al. (2014) Genetic crosses and complementation reveal essential functions for the Plasmodium stage-specific actin2 in sporogonic development. *Cell Microbiol* 16:751–767.
19. Vahokoski J, et al. (2014) Structural differences explain diverse functions of Plasmodium actins. *PLoS Pathog* 10:e1004091.
20. Hliscs M, et al. (2015) Organization and function of an actin cytoskeleton in Plasmodium falciparum gametocytes. *Cell Microbiol* 17:207–225.
21. Webb SE, et al. (1996) Contractile protein system in the asexual stages of the malaria parasite Plasmodium falciparum. *Parasitology* 112:451–457.
22. Kudryashev M, Lepper S, Baumeister W, Cyrklaff M, Frischknecht F (2010) Geometric constrains for detecting short actin filaments by cryogenic electron tomography. *PMC Biophys* 3:6.
23. Sidén-Kiamos I, Louis C, Matuschewski K (2012) Evidence for filamentous actin in ookinetes of a malarial parasite. *Mol Biochem Parasitol* 181:186–189.
24. Angrisano F, et al. (2012) A GFP-actin reporter line to explore microfilament dynamics across the malaria parasite lifecycle. *Mol Biochem Parasitol* 182:93–96.
25. Angrisano F, et al. (2012) Spatial localisation of actin filaments across developmental stages of the malaria parasite. *PLoS One* 7:e32188.
26. Mizuno Y, et al. (2002) Effect of jasplakinolide on the growth, invasion, and actin cytoskeleton of Plasmodium falciparum. *Parasitol Res* 88:844–848.
27. Schmitz S, et al. (2005) Malaria parasite actin filaments are very short. *J Mol Biol* 349: 113–125.
28. Bubb MR, Senderowicz AM, Sausville EA, Duncan KL, Korn ED (1994) Jasplakinolide, a cytotoxic natural product, induces actin polymerization and competitively inhibits the binding of phalloidin to F-actin. *J Biol Chem* 269:14869–14871.
29. Crews P, Manes LV, Boehler M (1986) Jasplakinolide, a cyclodepsipeptide from the marine sponge, *Jaspis* SP. *Tetrahedron Lett* 27:2797–2800.
30. Schmitz S, et al. (2010) Malaria parasite actin polymerization and filament structure. *J Biol Chem* 285:36577–36585.
31. Bubb MR, Spector I, Beyer BB, Fosen KM (2000) Effects of jasplakinolide on the kinetics of actin polymerization. An explanation for certain in vivo observations. *J Biol Chem* 275:5163–5170.
32. von der Ecken J, Heissler SM, Pathan-Chhatbar S, Manstein DJ, Raunser S (2016) Cryo-EM structure of a human cytoplasmic actomyosin complex at near-atomic resolution. *Nature* 534:724–728.
33. Löwe J, He S, Scheres SHW, Savva CG (2016) X-ray and cryo-EM structures of monomeric and filamentous actin-like protein MamK reveal changes associated with polymerization. *Proc Natl Acad Sci USA* 113:13396–13401.
34. Tannert R, et al. (2010) Synthesis and structure-activity correlation of natural-product inspired cyclodepsipeptides stabilizing F-actin. *J Am Chem Soc* 132:3063–3077.
35. Zabriskie TM, et al. (1986) Jaspamide, a modified peptide from a Jaspis sponge, with insecticidal and antifungal activity. *J Am Chem Soc* 108:3123–3124.
36. Visegrády B, Lorinczy D, Hild G, Somogyi B, Nyitrai M (2004) The effect of phalloidin and jasplakinolide on the flexibility and thermal stability of actin filaments. *FEBS Lett* 565:163–166.
37. Vig A, et al. (2011) The effect of toxins on inorganic phosphate release during actin polymerization. *Eur Biophys J* 40:619–626.
38. Ge P, Durer ZAO, Kudryashov D, Zhou ZH, Reisler E (2014) Cryo-EM reveals different coronin binding modes for ADP- and ADP-BeFx actin filaments. *Nat Struct Mol Biol* 21:1075–1081.
39. Fujii T, Namba K (2017) Structure of actomyosin rigour complex at 5.2 Å resolution and insights into the ATPase cycle mechanism. *Nat Commun* 8:13969.
40. Kortemme T, Baker D (2002) A simple physical model for binding energy hot spots in protein-protein complexes. *Proc Natl Acad Sci USA* 99:14116–14121.
41. Kortemme T, Kim DE, Baker D (2004) Computational alanine scanning of protein-protein interfaces. *Sci STKE* 2004:pl2.
42. Jacot D, et al. (2016) An apicomplexan actin-binding protein serves as a connector and lipid sensor to coordinate motility and invasion. *Cell Host Microbe* 20:731–743.
43. Grant T, Grigorieff N (2015) Measuring the optimal exposure for single particle cryo-EM using a 2.6 Å reconstruction of rotavirus VP6. *Elife* 4:e06980.
44. Hohn M, et al. (2007) SPARX, a new environment for Cryo-EM image processing. *J Struct Biol* 157:47–55.
45. Rohou A, Grigorieff N (2015) CTFFIND4: Fast and accurate defocus estimation from electron micrographs. *J Struct Biol* 192:216–221.
46. Pettersen EF, et al. (2004) UCSF Chimera–A visualization system for exploratory research and analysis. *J Comput Chem* 25:1605–1612.
47. Scheres SHW (2012) RELION: Implementation of a Bayesian approach to cryo-EM structure determination. *J Struct Biol* 180:519–530.
48. Sali A, Blundell TL (1993) Comparative protein modelling by satisfaction of spatial restraints. *J Mol Biol* 234:779–815.
49. Lopéz-Blanco JR, Chacón P (2013) iMODFIT: Efficient and robust flexible fitting based on vibrational analysis in internal coordinates. *J Struct Biol* 184:261–270.
50. Adams PD, et al. (2011) The Phenix software for automated determination of macromolecular structures. *Methods* 55:94–106.
51. Emsley P, Lohkamp B, Scott WG, Cowtan K (2010) Features and development of Coot. *Acta Crystallogr D Biol Crystallogr* 66:486–501.
52. Smart OS, et al. (2011) Grade Web Server Version v1.103. Available at grade.globalphasing.org and www.globalphasing.com. Accessed July 21, 2016.
53. Brown A, et al. (2015) Tools for macromolecular model building and refinement into electron cryo-microscopy reconstructions. *Acta Crystallogr D Biol Crystallogr* 71: 136–153.
54. Moriya T, et al. (2017) High-resolution single particle analysis from electron cryomicroscopy images using SPHIRE. *J Vis Exp*, 10.3791/55448.
55. Sievers F, et al. (2011) Fast, scalable generation of high-quality protein multiple sequence alignments using Clustal Omega. *Mol Syst Biol* 7:539.
56. Irwin JJ, Shoichet BK (2005) ZINC–A free database of commercially available compounds for virtual screening. *J Chem Inf Model* 45:177–182.
57. Nicholls RA, Fischer M, McNicholas S, Murshudov GN (2014) Conformation-independent structural comparison of macromolecules with ProSMART. *Acta Crystallogr D Biol Crystallogr* 70:2487–2499.
58. Chen VB, et al. (2010) MolProbity: All-atom structure validation for macromolecular crystallography. *Acta Crystallogr D Biol Crystallogr* 66:12–21.
59. Anandakrishnan R, Aguilar B, Onufriev AV (2012) H++ 3.0: Automating pK prediction and the preparation of biomolecular structures for atomistic molecular modeling and simulations. *Nucleic Acids Res* 40:W537–W541.
60. Hessa T, et al. (2005) Recognition of transmembrane helices by the endoplasmic reticulum translocon. *Nature* 433:377–381.
61. Pyrkov TV, Chugunov AO, Krylov NA, Nolde DE, Efremov RG (2009) PLATINUM: A web tool for analysis of hydrophobic/hydrophilic organization of biomolecular complexes. *Bioinformatics* 25:1201–1202.
62. Hayward S, Lee RA (2002) Improvements in the analysis of domain motions in proteins from conformational change: DynDom version 1.50. *J Mol Graph Model* 21:181–183.
63. Otterbein LR, Graceffa P, Dominguez R (2001) The crystal structure of uncomplexed actin in the ADP state. *Science* 293:708–711.
64. The UniProt Consortium (2017) UniProt: The universal protein knowledgebase. *Nucleic Acids Res* 45:D158–D169.